PHYSICAL REVIEW E **81**, 036322 (2010)

Influence of counter-rotating von Kármán flow on cylindrical Rayleigh-Bénard convection

Lyes Bordja,[1] Laurette S. Tuckerman,[2,*] Laurent Martin Witkowski,[3] María Cruz Navarro,[4] Dwight Barkley,[5] and Rachid Bessaih[6]

[1]*Faculté Sciences de l'Ingénieur, Département de Génie Mécanique, Université de Jijel, BP 98, Ouled Aissa, Jijel-18000, Algeria*

[2]*PMMH-ESPCI, CNRS (UMR 7636), Univ. Paris 6 & 7, 10 rue Vauquelin, 75231 Paris, France*

[3]*LIMSI–CNRS (UPR 3251) and UPMC Paris 6, 4 Place Jussieu, 75005, Paris, France*

[4]*Departamento de Matemáticas, Facultad de CC. Químicas, Universidad de Castilla La Mancha, Camilo José Cela s/n, 13071 Ciudad Real, Spain*

[5]*Mathematics Institute, University of Warwick, Coventry CV4 7AL, United Kingdom*

[6]*LEAP, Département de Génie Mécanique, Université Mentouri de Constantine, Route d'Aïn El Bey, 25000 Constantine, Algeria*

(Received 9 October 2009; published 26 March 2010)

The axisymmetric flow in an aspect-ratio-one cylinder whose upper and lower bounding disks are maintained at different temperatures and rotate at equal and opposite velocities is investigated. In this combined Rayleigh-Bénard/von Kármán problem, the imposed temperature gradient is measured by the Rayleigh number Ra and the angular velocity by the Reynolds number Re. Although fluid motion is present as soon as $\mathrm{Re} \neq 0$, a symmetry-breaking transition analogous to the onset of convection takes place at a finite Rayleigh number higher than that for $\mathrm{Re}=0$. For $\mathrm{Re} < 95$, the transition is a pitchfork bifurcation to a pair of steady states, while for $\mathrm{Re} > 95$, it is a Hopf bifurcation to a limit cycle. The steady states and limit cycle are connected via a pair of saddle-node infinite-period bifurcations except very near the Takens-Bogdanov codimension-two point, where the scenario includes global bifurcations. Detailed phase portraits and bifurcation diagrams are presented, as well as the evolution of the leading part of the spectrum, over the parameter ranges $0 \leq \mathrm{Re} \leq 120$ and $0 \leq \mathrm{Ra} \leq 30\,000$.

DOI: 10.1103/PhysRevE.81.036322 PACS number(s): 47.20.Ky, 47.20.Bp, 47.10.Fg, 47.32.Ef

I. INTRODUCTION

Thermal convection and shear are central to the study of hydrodynamic instabilities. The interest in these stems both from their large number of practical applications and also from their status as prototypes in theoretical investigation. In this study, we combine two well-known cylindrical configurations: Rayleigh-Bénard convection in which the upper and lower bounding disks of the cylinder are maintained at different temperatures, and von Kármán flow in which the disks rotate at equal and opposite velocities. We choose the simplest small-aspect-ratio geometry: a cylinder with equal height and radius, with imposed axisymmetry.

There is an extensive literature on Rayleigh-Bénard convection in a small to medium-aspect-ratio cylinder (in which the radius is between 0.5 and 5 times the height), e.g., [1–6]. The references most relevant to us are axisymmetric simulations [7–9] which produced patterns of radially traveling concentric rolls (target patterns). These were shown to be produced in most cases by a saddle-node infinite-period (SNIPER) bifurcation which will be the subject of much of the present investigation.

The literature on von Kármán flow is not as voluminous, but is growing. Restricting ourselves to the small to medium-aspect-ratio and the exactly or nearly exactly counter-rotating configuration, recent numerical articles include axisymmetric and non-axisymmetric simulations [10–16]. Interest in this problem has been enhanced by experiments using this configuration at high Reynolds numbers to generate turbulence [17,18] or a magnetic field via the dynamo effect [19–21].

The combined Rayleigh-Bénard/von Kármán configuration seems, however, unexplored. This situation stands in contrast to that of other shear and rotating flows. The superposition of plane Poiseuille flow with Rayleigh-Bénard convection (PRB), has been the subject of a great many investigations; indeed, a recent review [22] cites hundreds of articles. For longitudinal rolls in plane Poiseuille and Couette flows, the threshold remains unchanged [23,24]. For rolls transverse to the Poiseuille flow, the threshold increases and its nature changes from absolute to convective, e.g., [25]. In Taylor-Couette flow between cylinders at different temperatures, the nature of the instability also depends strongly on the angle between the imposed shear and buoyancy force, e.g., [26,27]. Turning to rotating disks, heat transfer in the rotor-stator configuration (between a rotating and a stationary disk) is extensively studied because of its applications to turbomachinery, e.g., [28]. Rotating Rayleigh-Bénard convection has long interested geophysicists, as well as researchers in pattern formation, e.g., [29], because of the possibility of chaos at onset; SNIPER bifurcations are found in this system as well [30,31]. Of the studies we have found of the flow between counter-rotating disks maintained at different temperatures, one computes the similarity solution between disks of infinite radius prior to the onset of convection [32], and another considers turbulent flows and neglects buoyancy [33].

The Rayleigh-Bénard/von Kármán problem in this geometry turns out to display a number of fascinating phenomena. For this reason, this problem has been used to develop and test a reduced model for numerical simulation, in which fields are expanded in terms of the eigenfunctions of the

*www.pmmh.espci.fr/~laurette; laurette@pmmh.espci.fr

governing equations linearized about a steady state; this study is the subject of a companion paper [34].

Our paper is organized as follows. Section II presents the governing equations of our configuration, along with the non-dimensionalizations we have used. In Sec. III, we describe the various codes we have used to carry out time-dependent simulations, branch continuation and linear stability analysis. Section IV shows how the transition threshold is affected by the disk counter-rotation. In Secs. V and VI, we present the steady states and limit cycles resulting from the transition. The connection between the steady states and limit cycle via a SNIPER bifurcation is explained in Sec. VII, which presents a complete phase diagram and bifurcation analysis. Reversing the traditional order, Sec. VIII gives a linear stability analysis of the basic state, showing how the convective eigenvalues and eigenvectors are interlaced and joined by the von Kármán flow.

II. PROBLEM FORMULATION

We consider a viscous Newtonian fluid governed by the Boussinesq approximation and contained in a cylinder of radius R and height H. The velocity and temperature fields are assumed axisymmetric. The bounding cylinder is stationary and thermally insulating. The upper and lower bounding disks are thermally conducting, rotate with angular velocities $+\Omega$ and $-\Omega$ and are held at temperatures T_0 and $T_0+\Delta T$, respectively. The nondimensional parameters are defined as

$$\mathrm{Re}=\frac{\Omega R^2}{\nu},\quad \mathrm{Ra}=\frac{g\gamma\Delta T R^3}{\alpha\nu},\quad \mathrm{Pr}=\frac{\nu}{\alpha},\quad \Gamma=\frac{R}{H} \tag{1}$$

where ν, α, γ, and g are the kinematic viscosity, the thermal diffusivity, the thermal-expansion coefficient, and the gravitational acceleration, respectively. The Prandtl number Pr and aspect ratio Γ are set to one. Reynolds numbers in the range $0\le\mathrm{Re}\le 120$ will be studied, along with Rayleigh numbers in the range $0\le\mathrm{Ra}\le 30\,000$.

Our study uses several independent codes, summarized in Sec. III, which use different non-dimensionalizations, and different problem formulations, i.e., primitive variables or streamfunction-vorticity. To facilitate later discussion, we briefly present these various formulations here. The nondimensionalized temperature is taken to be the deviation from T_0 divided by ΔT and lengths are nondimensionalized by R. The imposed counter-rotation of the disks provides a natural time scale: if time is nondimensionalized by $1/\Omega$ and velocities by $R\Omega$, the resulting governing equations are

$$\nabla\cdot\mathbf{U}=0, \tag{2a}$$

$$\partial_t\mathbf{U}+(\mathbf{U}\cdot\nabla)\mathbf{U}=-\nabla P+\frac{1}{\mathrm{Re}}\Delta\mathbf{U}+\frac{\mathrm{Ra}}{\mathrm{PrRe}^2}T\mathbf{e}_z, \tag{2b}$$

$$\partial_t T+\mathbf{U}\cdot\nabla T=\frac{1}{\mathrm{PrRe}}\nabla^2 T, \tag{2c}$$

where Δ and ∇^2 denote the vector and scalar Laplacian, respectively. The boundary conditions are

$$U_r=U_z=0,\quad U_\theta=+r,\quad T=0\ \text{at}\ z=1, \tag{3a}$$

$$U_r=U_z=0,\quad U_\theta=-r,\quad T=1\ \text{at}\ z=0, \tag{3b}$$

$$U_r=U_z=0,\quad U_\theta=0,\quad \partial_r T=0\ \text{at}\ r=1, \tag{3c}$$

$$U_r=\partial_r U_z=0,\quad U_\theta=0,\quad \partial_r T=0\ \text{at}\ r=0. \tag{3d}$$

These equations cannot be used in the absence of rotation, when $\mathrm{Re}=0$. To allow for this case, the unit of time can instead be taken to be the viscous diffusion time R^2/ν, with the resulting velocity scale ν/R. In addition, with the assumption of axisymmetry, the meridional velocity components (V_r,V_z) are best described by the Stokes streamfunction Ψ,

$$V_r\mathbf{e}_r+V_z\mathbf{e}_z=\frac{\mathbf{e}_r}{r}\partial_z\Psi-\frac{\mathbf{e}_z}{r}\partial_r\Psi=\frac{\mathbf{e}_\theta}{r}\times\nabla\Psi. \tag{4a}$$

Defining operators

$$\partial_\pm\equiv\partial_r\pm\frac{1}{r}, \tag{4b}$$

the azimuthal vorticity is:

$$D^2\Psi\equiv\frac{1}{r}\left(\nabla^2-\frac{2}{r}\partial_r\right)\Psi=\frac{1}{r}(\partial_-\partial_r+\partial_z^2)\Psi \tag{4c}$$

and the Navier-Stokes and Boussinesq equations reduce to

$$\partial_s D^2\Psi+(V_r\partial_-+V_z\partial_z)D^2\Psi=\left(\nabla^2-\frac{1}{r^2}\right)D^2\Psi-\frac{\mathrm{Ra}}{\mathrm{Pr}}\partial_r T+\partial_z\left(\frac{V_\theta^2}{r}\right), \tag{5a}$$

$$\partial_s T+(V_r\partial_r+V_z\partial_z)T=\frac{1}{\mathrm{Pr}}\nabla^2 T, \tag{5b}$$

$$\partial_s V_\theta+(V_r\partial_++V_z\partial_z)V_\theta=\left(\nabla^2-\frac{1}{r^2}\right)V_\theta. \tag{5c}$$

The rotation then appears in the boundary conditions, which become

$$\Psi=\partial_z\Psi=0\Leftrightarrow V_r=V_z=0,\quad V_\theta=+r\mathrm{Re},\quad T=0\ \text{at}\ z=1, \tag{6a}$$

$$\Psi=\partial_z\Psi=0\Leftrightarrow V_r=V_z=0,\quad V_\theta=-r\mathrm{Re},\quad T=1\ \text{at}\ z=0, \tag{6b}$$

$$\Psi=\partial_r\Psi=0\Leftrightarrow V_r=V_z=0,\quad V_\theta=0,\quad \partial_r T=0\ \text{at}\ r=1, \tag{6c}$$

$$\Psi=D^2\Psi=0\Leftrightarrow V_r=\partial_r V_z=0,\quad V_\theta=0,\quad \partial_r T=0\ \text{at}\ r=0. \tag{6d}$$

The velocity and time in Eqs. (2) and (3) are related to those in Eqs. (4)–(6) by $\mathbf{V}=\mathrm{Re}\mathbf{U}$ and $s=t/\mathrm{Re}$; the temperature T

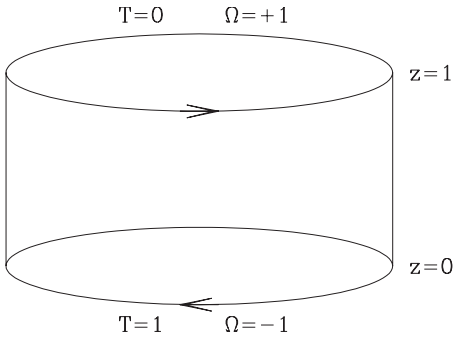

FIG. 1. Cylinder with height and radius equal to one. The bottom disk is heated and rotated in the clockwise direction, while the top disk is cooled and rotated in the counterclockwise direction.

and all lengths remain unchanged. Equations (5c) and (5b) can be considered to be advection-diffusion equations for the azimuthal velocity V_θ and the temperature T. Equation (5a) shows that gradients in V_θ and T in turn generate vorticity. The vertical gradient $\partial_z(V_\theta^2/r)$, when combined with boundary conditions (6a) and (6b), corresponds to Ekman pumping, by which the z-dependent V_θ generates meridional vorticity and velocity for any nonzero Re. This meridional velocity in turn affects the azimuthal velocity and the temperature via Eqs. (5c) and (5b). However, the thermal gradient term $\partial_r T$ in vorticity Eq. (5a) is radial, and so the axial temperature gradient imposed by boundary conditions in Eqs. (6a) and (6b) does not immediately impart motion to the fluid for any nonzero Ra. That is, Rayleigh-Bénard convection occurs via an instability at a finite threshold Ra_c, in contrast to natural convection, in which an externally imposed horizontal gradient generates motion for any $\mathrm{Ra}>0$ via the term $\mathrm{Ra}\,\partial_r T$.

Finally, we state the symmetries of the configuration of our problem, which can be seen from Fig. 1. The Rayleigh-Bénard convection problem has the symmetry of combined reflection in z and in T about their mean values, sometimes called the Boussinesq symmetry. The von Kármán flow has the symmetry of combined reflection in z and in θ, called R_π [15]. (In this axisymmetric problem, reflection in θ means only reversing the sign of U_θ; since all solutions are invariant under rotations in θ, these are not considered.) The Rayleigh-Bénard/von Kármán problem thus has the symmetry which combines reflection in z, θ, and T. A state is reflection-symmetric if it is invariant under the reflection operator defined in the two formulations by

$$\kappa:\begin{pmatrix} U_r \\ U_\theta \\ U_z \\ T \end{pmatrix}(r,z) \equiv \begin{pmatrix} U_r \\ -U_\theta \\ -U_z \\ 1-T \end{pmatrix}(r,1-z) \quad \text{or}$$

$$\kappa:\begin{pmatrix} \Psi \\ U_\theta \\ T \end{pmatrix}(r,z) \equiv \begin{pmatrix} -\Psi \\ -U_\theta \\ 1-T \end{pmatrix}(r,1-z). \tag{7}$$

III. NUMERICAL METHODS

We have solved the governing equations using a number of different codes. The first is the time-integration code written by Patankar [35] for Eqs. (2) and (3). The temporal discretization uses the backward differentiation formula for the time derivative, the explicit Adams-Bashforth formula for the advective and buoyancy terms, and implicit evaluation of the diffusive terms, which leads to the following form for time stepping Eq. (2):

$$\begin{aligned}
&\frac{1}{2\Delta t}\left[3\begin{pmatrix}\mathbf{U}\\ T\end{pmatrix}^{t+\Delta t} - 4\begin{pmatrix}\mathbf{U}\\ T\end{pmatrix}^{t} + \begin{pmatrix}\mathbf{U}\\ T\end{pmatrix}^{t-\Delta t}\right] \\
&\quad + 2\begin{pmatrix}(\mathbf{U}\cdot\nabla)\mathbf{U}\\ \mathbf{U}\cdot\nabla T\end{pmatrix}^{t} - \begin{pmatrix}(\mathbf{U}\cdot\nabla)\mathbf{U}\\ \mathbf{U}\cdot\nabla T\end{pmatrix}^{t-\Delta t} \\
&= \begin{pmatrix}\frac{1}{\mathrm{Re}}\Delta\mathbf{U}\\ \frac{1}{\mathrm{PrRe}}\nabla^2 T\end{pmatrix}^{t+\Delta t} - \begin{pmatrix}\nabla P\\ 0\end{pmatrix}^{t+\Delta t} \\
&\quad + 2\begin{pmatrix}\frac{\mathrm{Ra}}{\mathrm{PrRe}^2}T\mathbf{e}_z\\ 0\end{pmatrix}^{t} - \begin{pmatrix}\frac{\mathrm{Ra}}{\mathrm{PrRe}^2}T\mathbf{e}_z\\ 0\end{pmatrix}^{t-\Delta t}.
\end{aligned}$$

The spatial discretization uses centered finite differences. A staggered grid is used, with pressure and temperature represented on the nodes and the velocity components between the nodes. A time step $\Delta t = 10^{-3}$ and a resolution in the radial and axial direction of 82×82 were used.

Time integration has also been carried out with a second code, which uses the streamfunction-vorticity formulation of Eqs. (4)–(6), a second-order finite difference scheme in space, and an alternating-direction-implicit scheme in time [36]. A 51×51 grid with a typical time step of $\Delta s = 10^{-4}$ were found to be adequate for obtaining converged results.

We also carried out bifurcation and linear stability analysis. We followed branches via Newton's method and calculated eigenvalues via ARPACK. Several different spatial representations have been used. One code uses the same spatial discretization, i.e., the streamfunction-vorticity formulation and the same spatial resolution, as the time-integration code mentioned in the previous paragraph. The Jacobian of the matrix built in the last step of Newton iteration is directly used in ARPACK in shift-invert mode. The branches are followed using an arclength continuation as described in [37] and the practical implementation of bordered matrix inversion can be found in [38].

The second code [39] with which we carried out bifurcation and linear stability analysis uses the primitive variable formulation and a pseudospectral spatial discretization. The number of Chebyshev polynomials (or Gauss-Lobatto collocation points) used is 15 in each of the r and z directions.

The quantitative results which we present have been obtained by two or more of the codes described above, and have also been verified by varying the resolution.

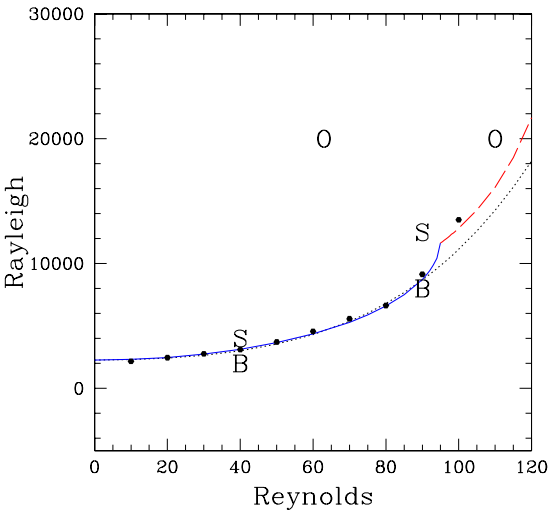

FIG. 2. (Color online) Convection thresholds as a function of Reynolds number. Solid blue curve: transition to steady convection. Dashed red curve: transition to oscillatory convection. Dotted black curve: fit to even fourth-order polynomial [Eq. (9)]. Points: thresholds obtained from time-dependent code. Letters indicate parameter values for flows presented in Figs. 3 and 4 (B, basic state), Figs. 5 and 6 (S, steady convection), and Figs. 7 and 8 (O, oscillatory convection).

IV. THRESHOLDS

In the absence of rotation, i.e., Re=0, the governing equations have as a solution the conductive state, in which the fluid is stationary and the temperature varies linearly in the vertical direction,

$$\mathbf{U} = 0, \quad T = 1 - z. \tag{8}$$

Although the conductive solution exists for all Ra, it loses stability at some critical value Ra_c to a convective solution, in which fluid motion ensues, breaking Boussinesq reflection symmetry (7). In the von Kármán system, as mentioned in Sec. II, Ekman pumping leads to recirculating regions for any nonzero value of Re. However, for a fixed value of Re, there is still a transition at a well-defined Ra_c, at which one solution loses stability to another. By analogy with the nonrotating case, we will call these the *basic* and *convective* solutions, despite the presence of fluid motion (and thus of convective heat transfer) for $\mathrm{Ra} < \mathrm{Ra}_c$, and we will continue to refer to the transition between them as the onset of convection.

We begin by showing the critical Rayleigh number for onset of axisymmetric convection as a function of Reynolds number. For $\mathrm{Re} < 95$, the bifurcation is to a steady state (i.e., the critical eigenvalue is real), and for $\mathrm{Re} > 95$, the bifurcation is to an oscillatory state (i.e., the critical eigenvalue is complex). The thresholds in Fig. 2 are obtained by calculating the eigenvalues of the linearized problem for fixed values of (Re,Ra) and interpolating to find the value $\mathrm{Ra}_c(\mathrm{Re})$ at which the eigenvalue or its real part crosses zero. Thresholds were also obtained independently by fitting decay rates from the time-stepping code to exponentials and extrapolating these to zero.

Away from where the bifurcation changes its nature from steady to oscillatory, Ra_c should be a smooth function of Re. In fact, Ra_c must be an even function of Re, since reversing Re means reversing the direction of rotation of the upper and lower disks, an operation which leaves all dynamical properties unchanged, as was argued [25] in the context of Rayleigh-Bénard convection with through flow. We fit Ra_c over the range of the steady bifurcation, $0 \le \mathrm{Re} \le 94$, to an even polynomial, obtaining:

$$\mathrm{Ra}_c \approx 2260 + (0.6243 \times \mathrm{Re})^2 + (0.0840 \times \mathrm{Re})^4. \tag{9}$$

We see that the von Kármán flow stabilizes the system against thermal convection. We contrast this with results from other mixed thermal/shear systems. In plane Poiseuille and Couette flow, the threshold for onset of longitudinal rolls is unaffected by the shear [23,24]. (In our system, the rolls can be seen as longitudinal, since the axes of concentric rolls are azimuthal, as is the velocity of the bounding disks.) In Taylor-Couette flow (measured by the Taylor number Ta) with a radial temperature gradient (measured by the Grashof number Gr), the role of rotation and heating are reversed from our system. Any radial temperature gradient causes large-scale motion (a role played by Re in our system) and a bifurcation to Taylor vortices is seen at a finite rotation rate (a role played by Ra in our system). In experiments on this system [26], Ta_c decreases with Gr, in contrast to the increase in Ra_c with Re in our case.

The threshold value $\mathrm{Ra}_c(\mathrm{Re}=0)=2260$ agrees well with those previously reported for the onset of convection for insulating sidewalls and aspect ratio $\Gamma=1$, notably 2260 [1,3], 2300 ($\Delta\mathrm{Ra}_c/\mathrm{Ra}_c=1.8\%$) [4], 2241 ($\Delta\mathrm{Ra}_c/\mathrm{Ra}_c=0.8\%$) [5], and 2250 ($\Delta\mathrm{Ra}_c/\mathrm{Ra}_c=0.4\%$) [6]. These authors all found the most unstable mode to be axisymmetric for cylindrical convection at this aspect ratio.

Varying Re and investigating the thresholds of nonaxisymmetric eigenmodes shows that the critical azimuthal wave number is $m=2$ for $\mathrm{Re} \ge 54.8$. At Re=0, the primary axisymmetric convective branch becomes unstable to an $m=2$ perturbation near Ra=3000 [4,5]. For the pure von Kármán flow, i.e., with Ra set to zero and Re gradually increased from zero, the first instability occurs near Re=300 to an $m=2$ mode [15]. We nonetheless restrict our consideration here to the axisymmetric bifurcations and eigenmodes. There are a number of reasons for doing so. First, an understanding of the axisymmetric problem is important for completeness: branches which are unstable may nonetheless play a role in the dynamics. Second, the axisymmetric problem displays a number of fascinating phenomena, both linear and nonlinear, as we will see. Because of this, it has served as a test case for a numerical method using a reduced model [34]; a presentation of the results from fully resolved computations is a necessary complement to this study. Finally, additional physical effects, e.g., magnetic fields, can stabilize the axisymmetric configuration [40].

V. STEADY CONVECTIVE STATES

We now discuss the nature of the steady flows below and above the convection threshold. The basic state, which is the

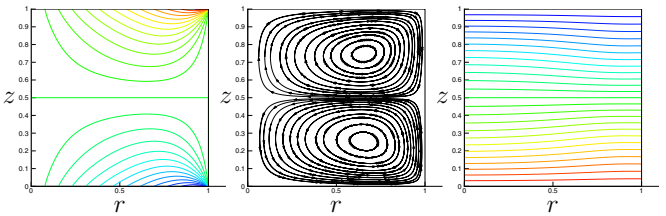

FIG. 3. (Color online) Basic flow at Re=40, Ra=2000. From left to right: U_θ, Ψ, and t T. Ranges for U_r and U_z are $[-0.05, 0.05]$ and $[-0.04, 0.04]$, respectively.

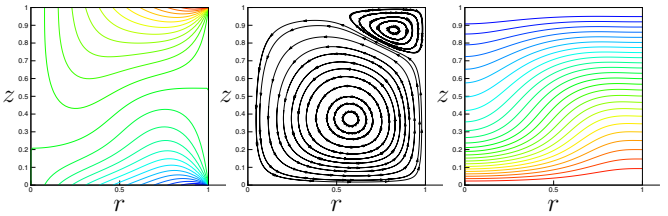

FIG. 5. (Color online) Convective state at Re=40, Ra=4000. From left to right: U_θ, Ψ, and T. Ranges for U_r and U_z are $[-0.11, 0.19]$ and $[-0.29, 0.11]$, respectively.

analog of the conductive state in the presence of von Kármán flow, is shown in Figs. 3 and 4 for Re=40, Ra=2000 and for Re=90, Ra=8000, respectively. The azimuthal velocity increases gradually from negative in the lower half to positive in the upper half of the cylinder, following the counter-rotating disks. It is singular at the corners $r=1$, $z=0,1$ since the boundary conditions are discontinuous where the stationary cylinder meets the rotating disks. The large recirculating cells caused by Ekman pumping are prominent features in the (r,z) plane, carrying fluid radially outward along both rotating disks at $z=0,1$, then along the bounding cylinder, inwards along the midplane $z=1/2$, and back toward the two disks along the axis. The azimuthal velocity and recirculating cells combine to yield fluid trajectories which are toroidal.

We may compare the basic flows in Figs. 3 and 4. For Re=90, the temperature field is noticeably different from linear conductive profile of Eq. (8). The recirculating cells are stronger, with a maximal velocity of $|U_r^{\max}|=0.11$, as compared to $|U_r^{\max}|=0.04$ for Re=40. These stronger recirculating cells exert more influence on the temperature field. At $r=1$, the isotherms are deviated toward the midplane as warm fluid converges upwards from the lower disk and cold fluid downwards from the upper disk. At $r=0$, the isotherms are deviated again, here outwards toward the upper and lower disks. The azimuthal velocity gradients for Re=90 are more concentrated near the disks. The basic states shown in Figs. 3 and 4 are reflection-symmetric about the midplane: each is invariant under κ, as defined in Eq. (7).

The transition to convection breaks the reflection symmetry. In the absence of rotation, the transition occurs at Ra =2260, as stated in Sec. IV, and leads to a single roll which occupies the entire cavity. For Re=40, transition occurs at $\mathrm{Ra}_c=3125$ and the resulting convective state, shown in Fig. 5 for Ra=4000, has one small roll (due to the weak von Kármán flow) in the upper right corner in addition to the main large convection roll. For Re=90, the onset of convection occurs at Ra=8622 and the resulting convective state is shown in Fig. 6 at Ra=12 500. The influence of the counter-rotating disks is stronger than it is at Re=40 and so the recirculating rolls, resulting from the combined effects of Ekman pumping (which favors two equal rolls) and convection (which favors a single roll), are more equal in size. The consequences on U_θ and T of these changes in Ψ can also clearly be seen in Figs. 5 and 6. (These in turn affect Ψ via the buoyancy and Ekman pumping effects, though to a lesser extent.)

Although the smaller cell in Figs. 5 and 6 is in the upper corner of the cylinder, the pitchfork bifurcation can produce a small cell at either the upper or lower corner. The breaking of reflection symmetry is also manifested by the azimuthal velocity: the $U_\theta=0$ contour intersects the axis near $z=0.2$ in both Figs. 5 and 6, in contrast to the basic flow, for which this contour is a straight line across the midplane at $z=0.5$.

VI. OSCILLATORY CONVECTIVE STATES

For Re>95, the transition from the basic state is a Hopf bifurcation, creating oscillatory flows. We fix Ra=20 000 and present two oscillatory states, or limit cycles, one at Re=110 in Fig. 7 and one at Re=63 in Fig. 8. (Although for Re=63, the first bifurcation as Ra is increased is to steady convection, there is another bifurcation at higher Ra to oscillatory convection and the resulting limit cycles are stable and connected to those created by the Hopf bifurcation for Re >95, as we will see in Sec. VII.) We call the limit cycles at Re=110 and Re=63 near-sinusoidal and near-heteroclinic, respectively, which we will also explain in Sec. VII.

Figures 7 and 8 show meridional vortices jostling with one another. At Re=110 (Fig. 7), the vortices are somewhat similar in size, with the vortex in the upper or lower outer

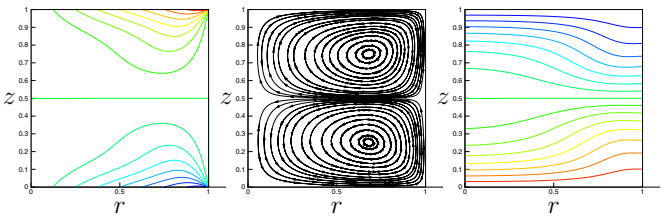

FIG. 4. (Color online) Basic flow at Re=90, Ra=8000. From left to right: U_θ, Ψ and T. Ranges for U_r and U_z are $[-0.11, 0.11]$ and $[-0.07, 0.07]$, respectively.

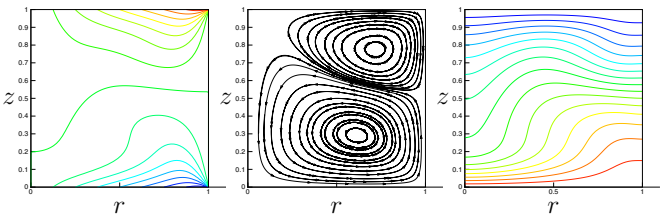

FIG. 6. (Color online) Convective state at Re=90, Ra=12 500. From left to right: U_θ, Ψ, and T. Ranges for U_r and U_z are $[-0.15, 0.18]$ and $[-0.24, 0.10]$, respectively.

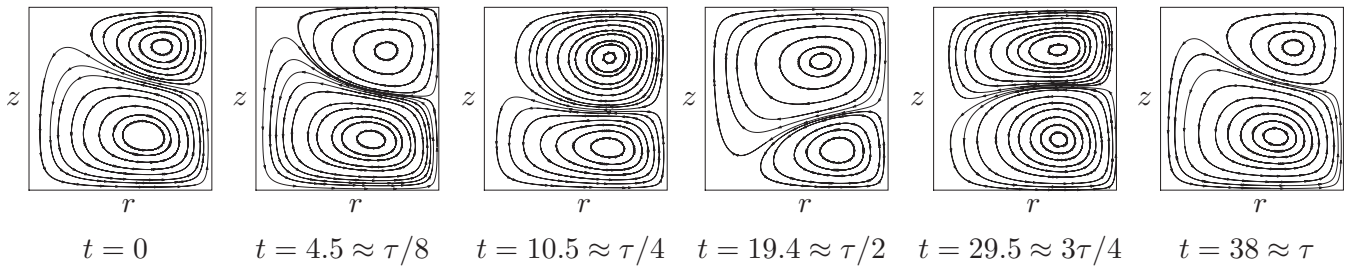

FIG. 7. Near-sinusoidal limit cycle at Ra=20 000, Re=110. Ψ is shown at times near 0, $\tau/8$, $\tau/4$, $\tau/2$, $3\tau/4$, τ indicated on time series in Fig. 9. Times are given in units of $1/\Omega$. The overall limit cycle has reflection symmetry: the states in the second half of the cycle are related by reflection symmetry to those in the first half of the cycle. The vortex in the upper right corner is smaller during the first half of the cycle and larger during the second half. The streamfunction contours are not equally spaced, but instead chosen to illustrate topological features of the flow.

corner alternatively becoming smaller and larger. At Re=63 (Fig. 8), the principle vortex remains much larger throughout the limit cycle, with much smaller vortices on the periphery. At $t=71.0$, there appear to be two vortices which both extend over the entire height, suggesting an interpretation of this limit cycle as a competition between one and two concentric radial vortices. This interpretation will be discussed further in Sec. VIII.

Section V showed that the transition to steady convection breaks the reflection symmetry, creating two asymmetric states related by the reflection operator κ. The transition to oscillatory convection has an analogous property: each of the instantaneous states shown in Figs. 7 and 8 is asymmetric,and the second half of each limit cycle is related to the first half by reflection, i.e.,

$$(U_r, U_\theta, U_z, T)(t+\tau/2) = \kappa(U_r, U_\theta, U_z, T)(t), \qquad (10)$$

where τ is the oscillation period.

To better understand the limit cycles in Figs. 7 and 8, we plot various scalar quantities, $U_z(0.16,0.5)$, $U_\theta(0.08,0.5)$, and $T(0.16,0.5)$, as a function of time and of each other to create the time series and phase portraits of Fig. 9. Figure 9 clearly shows the very different character of the limit cycles at Re=110 and Re=63. At Re=110, the time series is fairly close to harmonic, and the phase portrait shows that the limit cycle is traversed at a fairly constant speed. In contrast, at Re=63, the time series shows two phases during which change is very slow, punctuated by abrupt transitions. The phase portrait corroborates this: two regions of the limit cycle show a dense accumulation of points, indicating a slow traversal of these regions.

We have seen that the period at Re=63 is about three times that at Re=110; it in fact approaches infinity as Re is decreased. (The approach by τ to infinity implies that it is extremely sensitive to any change in the physical or numerical parameters. Thus, values of τ are subject to a great deal of uncertainty.) This is demonstrated in Fig. 10, which plots the dependence of the square frequency (inverse square period) on Re for Ra=20 000 and for Ra=18 000, for two different scalings: with the disk rotation period $1/\Omega$ (left) and with the viscous diffusion time R^2/ν (right).

VII. BIFURCATION DIAGRAM

We have mentioned several features of the oscillatory states in Sec. VI:

(i) the small vortex does not remain in the upper or lower corner, as it does for the steady convective states, but alternates between the two locations, as shown in Figs. 7 and 8;

(ii) the character of the oscillations varies substantially, from near-sinusoidal to relaxational (plateaus punctuated by fast changes) as shown in Fig. 9; and

(iii) the period varies substantially with changes in Re or Ra, as shown in Fig. 10.

All of these features are typical of the bifurcation scenario we will now describe, and which is illustrated in Fig. 11.

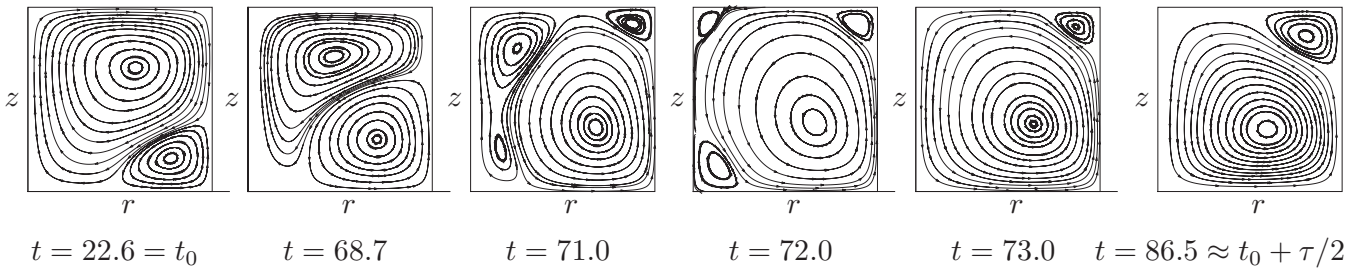

FIG. 8. Near-heteroclinic limit cycle at Ra=20 000, Re=63. Ψ is shown at times indicated on time series in Fig. 9: $t=22.6$; four instants in $68 \le t \le 73$, during which the flow changes a great deal; and $t=86.5$, approximately a half-period $\tau/2 \approx 57.5$ after $t=22.6$. The vortex in the lower right corner grows and the vortex in the upper left corner folds and then divides into three small vortices. Two of these disappear, leaving a small vortex in the upper right corner. As in Fig. 7, the states in the second half of the cycle are related by reflection symmetry to those in the first half of the cycle and the streamfunction contours are chosen to illustrate topological features of the flow.

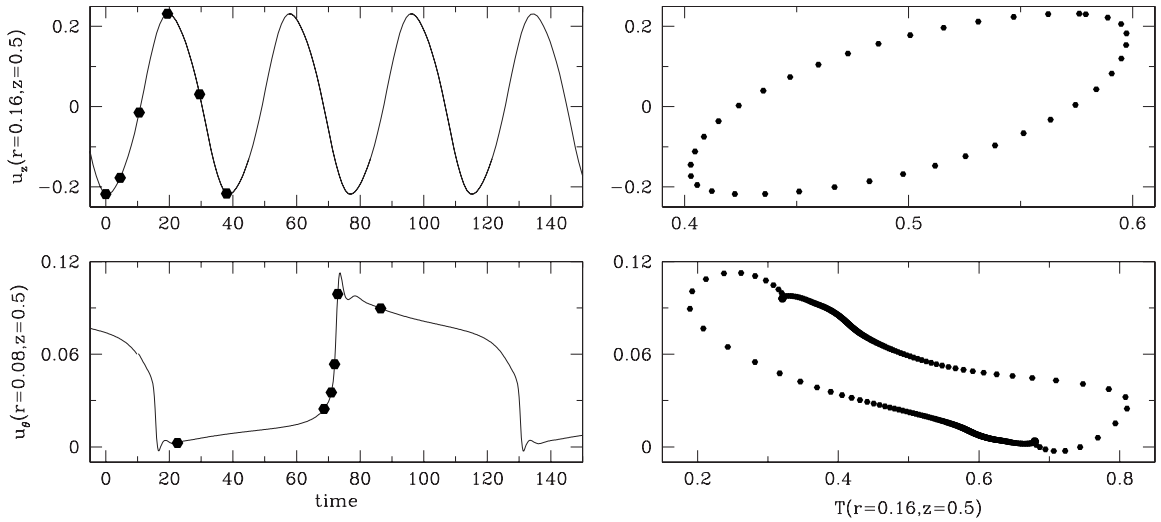

FIG. 9. Time series (left) and phase portraits (right) corresponding to limit cycles at Ra=20 000. Dots in time series refer to visualizations in Figs. 7 and 8. Dots in phase portraits are plotted at equally spaced times so that their density reflects the rate at which the limit cycle is traversed. Top: at Re=110, the oscillations are regular and near-sinusoidal. Bottom: at Re=63, the oscillations have a much longer period and consist mainly of two long plateaus with abrupt gradients between them.

For Re$<$95, the threshold for convection, already shown in Fig. 2, corresponds to a pitchfork bifurcation PF_1. For Ra below PF_1, i.e., inset (a) in Fig. 11, the only solution is the basic flow, an example of which is given in Fig. 3. Proceeding clockwise, at PF_1, the basic state loses stability and gives rise to two symmetrically-related convective states, as illustrated in inset (c) and Fig. 5. A second pitchfork bifurcation, PF_2, occurs at a higher value of Ra. For Ra between curves PF_2 and SN, in regions (d) and (e), there exist two additional steady states, both unstable and also related by symmetry operation (7). The trajectories leaving the two unstable states terminate on the two stable states, forming an invariant set that resembles a circle or ellipse. Leaving PF_2 and approaching SN, as shown in (e), the two stable and unstable states approach one other along this invariant set, finally merging and annihilating one another in two symmetrically-related saddle-node bifurcations at SN.

Exactly at SN, trajectories spend an infinite-period of time at the two locations at which the stable and unstable states merged, forming a limit cycle whose period is infinite: a heteroclinic cycle. For Ra above SN, but sufficiently nearby, as in inset (f), much of the time during the limit cycle is spent in the neighborhood of the former fixed points, as shown for Re=63, Ra=20 000 in Fig. 8 and in the bottom half of Fig. 9. Leaving SN, by increasing Ra or Re, as in inset (g), the time spent in the vicinity of these points shortens, and the period decreases, as shown for Re=110, Ra=20 000 in Fig. 7 and in the upper half of Fig. 9. Finally, for Re$>$95, curve H corresponds to a Hopf bifurcation, below which the basic state is a stable spiral focus, as in inset (b).

Although the saddle-node bifurcation signals the merging of two pairs of steady states, it results in a limit cycle because of the connections between these steady states.

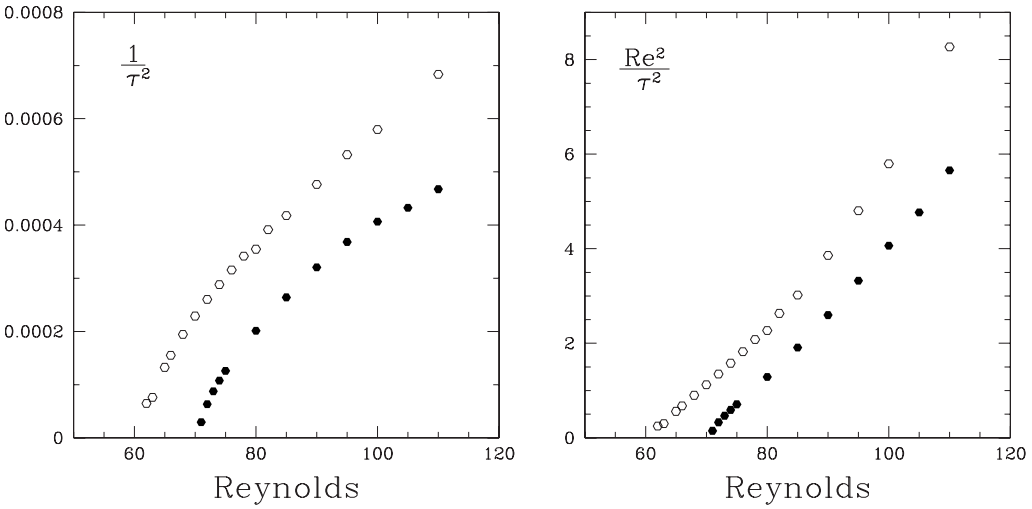

FIG. 10. Variation in square frequency with Re. Left: $1/\tau^2$ for Ra=20 000 (hollow dots) and for Ra=18 000 (solid dots). Right: $(Re/\tau)^2$ for Re=20 000 (hollow dots) and for Ra=18 000 (solid dots).

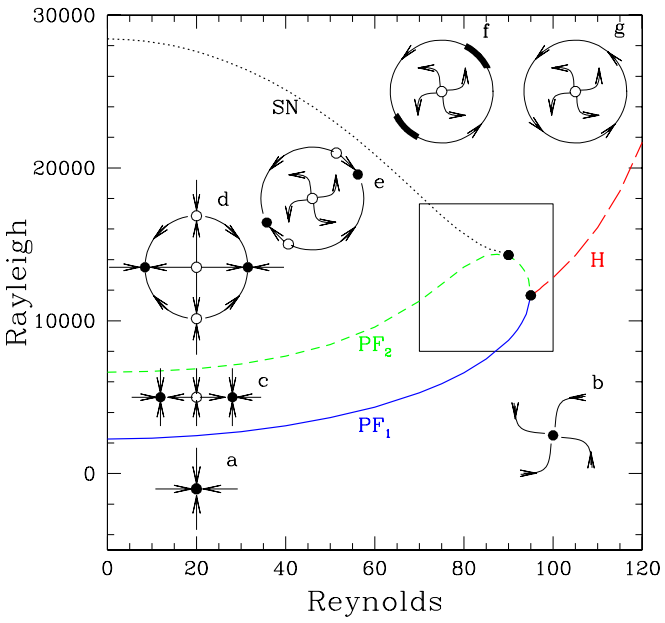

FIG. 11. (Color online) Curves of bifurcation points in the (Re,Ra) plane showing first pitchfork (blue, solid, PF_1), second pitchfork (green, short-dashed, PF_2), Hopf (red, long-dashed, H), and saddle-node (black, dotted, SN) bifurcations. Dots indicate codimension-two points, where curve PF_2 meets curves SN (90,14 300) and H (95,11 750). An enlargement of the region inside the square is shown in Fig. 12. Phase portraits shown as insets. (a) and (b) Below PF_1 and H, the only solution is the stable basic flow, which is (a) a node or (b) a spiral focus. (c) Between PF_1 and PF_2, the basic flow is unstable and there exist two stable asymmetric convective states. (d) and (e) Between PF_2 and SN, there exist five states: the unstable basic flow and two stable and two unstable convective states. (f) and (g) Between SN and H, the unstable basic flow is surrounded by a stable limit cycle, which is near-heteroclinic near SN (f) and near-sinusoidal near H (g).

(These connections in turn result from the formation of the steady states via two successive pitchfork bifurcations.) Under these circumstances, the saddle-node bifurcation is called a SNIPER, for saddle-node in a periodic orbit, or saddle-node infinite-period; other names are a saddle-node homoclinic, a SNIC (saddle-node on invariant circle), or an Andronov bifurcation [41,42]. It can be shown that, near a SNIPER bifurcation, the period τ of the limit cycle varies like

$$\frac{1}{\tau^2} \sim \mu - \mu_c \tag{11}$$

where $\mu-\mu_c$ can be either $\mathrm{Ra}-\mathrm{Ra_{SN}}$ for fixed Re or $\mathrm{Re}-\mathrm{Re_{SN}}$ for fixed Ra or any combination of the two. Although the square frequency is proportional to the distance from threshold sufficiently near the threshold for any scaling, Fig. 10 shows that, for our case, relation (11) holds over a wider range of Re when τ is scaled by the viscous diffusion time (right) than when it is scaled by the disk rotation period (left).

Figure 11 shows two codimension-two points. At (95,11 750), curves H, PF_1 and PF_2 meet in a Takens-Bogdanov (TB) point. At (90,14 300), curve SN terminates on PF_2 at a hysteresis point, where the pitchfork bifurcation changes from supercritical to subcritical. (Because the TB point was calculating using eigenvalue computations rather than by specialized algorithms such as those in [38], we have been able to determine its location only to within about 0.5% in Re and 5% in Ra.) Between these two points, Fig. 11 shows curve PF_2 separating region (c), in which the unstable basic state coexists with two stable steady states, and region (f,g) in which it coexists with a stable limit cycle. The pitchfork bifurcation PF_2 cannot bring about such a transition. [The other paths between (c) and (f,g), either clockwise through PF_2, region (d,e), and SN; or counterclockwise through PF_1, region (a,b), and H, can bring about this transition.] This means that Fig. 11 is incomplete. The solution is to be found in the normal form of the Takens-Bogdanov codimension-two point in the presence of reflection symmetry [42,43],

$$\frac{dx}{dt} = y, \tag{12a}$$

$$\frac{dy}{dt} = -\mu_1 x + \mu_2 y - \delta x^3 - x^2 y, \tag{12b}$$

where $\delta = \pm 1$. We take $\delta=+1$, since it is this choice which reproduces the phenomena we see in the fluid-dynamical simulation.

The behavior of normal form (12) is illustrated in Fig. 12 (right) and in Table I. The TB codimension-two point is located at $(\mu_1,\mu_2)=(0,0)$ and the basic state at $(x,y)=(0,0)$. The basic state undergoes a pitchfork bifurcation ($\lambda_+=0$), analogous to our PF_1 and PF_2, at $\mu_1=0$ and a Hopf bifurcation [$\mathcal{R}e(\lambda_\pm)=0$], analogous to our H at $\mu_2=0$ for $\mu_1>0$. Additionally, Table I shows that the solutions $(\pm\sqrt{|\mu_1|},0)$ undergo a Hopf bifurcation at $\mu_2=-\mu_1$ for $\mu_1<0$. Indeed, we have calculated a secondary Hopf bifurcation (SH) for the hydrodynamic system, and indicate it in Fig. 12. This bifurcation is subcritical and the limit cycles it generates are unstable. Arnold [42,43] showed that system (12) contains two additional bifurcation curves emanating from the codimension-two point $(\mu_1,\mu_2)=(0,0)$, one a gluing bifurcation, G, and the other a sadde-node of periodic orbits, SNP. Although the curves SNP and G correspond to global bifurcations and cannot be calculated by examination of the eigenvalues in Table I, they have been determined [42] to be $\mu_2=-0.752\mu_1$ for SNP and $\mu_2=-0.8\mu_1$ for G. (We have computed neither for our hydrodynamic system.) Together, bifurcations SNP, G, SH, and P accomplish the transformation in the small square of Fig. 11, between the three steady states of region (c) to the stable limit cycle of region (g).

TABLE I. Properties of the Takens-Bogdanov normal form.

Steady state	Jacobian	Eigenvalues
(0,0)	$\begin{pmatrix} 0 & 1 \\ \mu_1 & \mu_2 \end{pmatrix}$	$\lambda_\pm = \frac{1}{2}\mu_2 \pm \sqrt{\frac{1}{4}\mu_2^2 - \mu_1}$
$(\pm\sqrt{\lvert\mu_1\rvert},0)$	$\begin{pmatrix} 0 & 1 \\ 2\mu_1 & \mu_2+\mu_1 \end{pmatrix}$	$\lambda_\pm = \frac{1}{2}(\mu_2+\mu_1) \pm \sqrt{\frac{1}{4}(\mu_2+\mu_1)^2 + 2\mu_1}$

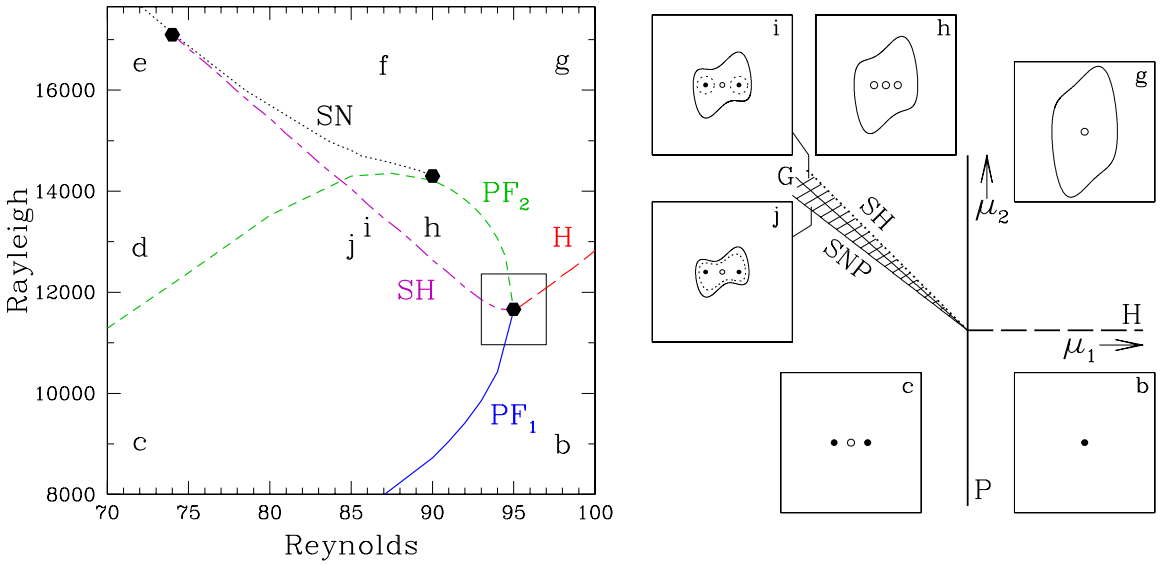

FIG. 12. (Color online) Left: enlargement of square in Fig. 11. The additional curve (violet, dash-dotted) indicates the secondary Hopf bifurcation SH which exists between codimension-two points (95,11 750) (where it meets H) and (74,17 100) (where it meets SN). Labels correspond to those of Fig. 11. Behavior in the square is described by TB normal form (12). Right: behavior of TB normal form (12). Shown are the pitchfork bifurcation P, Hopf bifurcation H, secondary Hopf bifurcation SH, as well as the saddle-node of periodic orbits SNP and the gluing bifurcation G which are contained in the unfolding of the TB point. Phase portraits (b), (c), (g) as in Fig. 11. (h) Between P and SH a stable limit cycle surrounds the unstable basic and convective flows. (i) Between SH and G, small unstable limit cycles surround each stable convective state. (j) Between G and SNP, two large limit cycles, one stable and one unstable, surround the three steady states. Hatched region indicates bistability between limit cycle and steady states.

We describe the bifurcations and phase portraits in Fig. 12, proceeding around the TB point in the counterclockwise direction. In region (b), the only solution is the stable basic state. The Hopf bifurcation H destabilizes the basic state and generates a stable limit cycle (g). The pitchfork bifurcation P is subcritical, and generates two unstable asymmetric states while reducing the number of unstable directions of the basic state from two to one (h). The secondary Hopf bifurcation SH is also subcritical, stabilizing the two asymmetric states while creating unstable limit cycles encircling each one (i). The gluing bifurcation G joins these two limit cycles to the symmetric state in a figure eight which, afterwards, form a single unstable limit cycle encircling all three steady states (j). Curves SH and SNP delineate a narrow wedge in which there is bistability between the limit cycle and the steady convective states. The stable and unstable limit cycles annihilate in a saddle-node of periodic orbits SNP, leaving only the unstable basic flow and the stable asymmetric steady states (c). In crossing the pitchfork bifurcation P, we return to the single stable symmetric state of b). Figure 12 shows a third codimension-two point where SH and SN meet at (74,17100). Other codimension-two points which we have not located must mark the ends of curves G and SNP as well.

Although the analysis surrounding the TB point is important for completeness, we emphasize that, over most of the (Re,Ra) plane, it is the SNIPER bifurcation which marks the boundary between steady and oscillatory convection; other bifurcations come into play only between (95,11 750) and (74,17 100).

Figure 13 shows representative bifurcation diagrams. Branches are labeled by their stability index, i.e., the number of eigenvalues with positive real parts. The stability index changes by one at a pitchfork bifurcation (for the basic state) or a saddle-node bifurcation and by two for a Hopf bifurcation. We plot the temperature at a fixed point $\bar{T} \equiv T(r=1/2,\ z=1/2)$ as a function of Ra for fixed Re along the bottom of the figure, and as a function of Re for fixed Ra along the right. To represent limit cycles, we plot $[\frac{1}{\tau}\int_0^\tau \bar{T}(t)^2 dt]^{1/2}$, the L_2 norm of $\bar{T}$ over an oscillation period τ. The three codimension-two points at (74,17 100), (90,14 300), and (95,11 750) and the limits of the pitchfork and saddle-node curves (Ra=2260 and 28 445) delimit the ranges over which different types of bifurcation diagrams occur.

(i) Re=60 represents the large typical range $0 \leq \mathrm{Re} \leq 74$: two successive supercritical pitchfork bifurcations generate two pairs of steady states which are annihilated by a saddle-node (SNIPER) bifurcation, leading to a limit cycle;

(ii) Re=85 represents [74,90]: secondary Hopf bifurcations have been added to the diagrams;

(iii) Re=93 represents [90,95]: the second pitchfork bifurcation has become subcritical;

(iv) For $\mathrm{Re} > 95$ (not shown), there are no nontrivial steady states and a Hopf bifurcation leads directly to the limit cycle;

(v) Ra=5000 represents the range $2260 \leq \mathrm{Ra} \leq 6640$: a single pitchfork bifurcation leads to a pair of steady states as Re decreases;

(vi) Ra=7000 represents [6640,11 750]: an additional pitchfork bifurcation and pair of steady branches can be seen;

(vii) Ra=13 000 represents [11 750,14 300]: a primary and two secondary Hopf bifurcations have been added to the scenario;

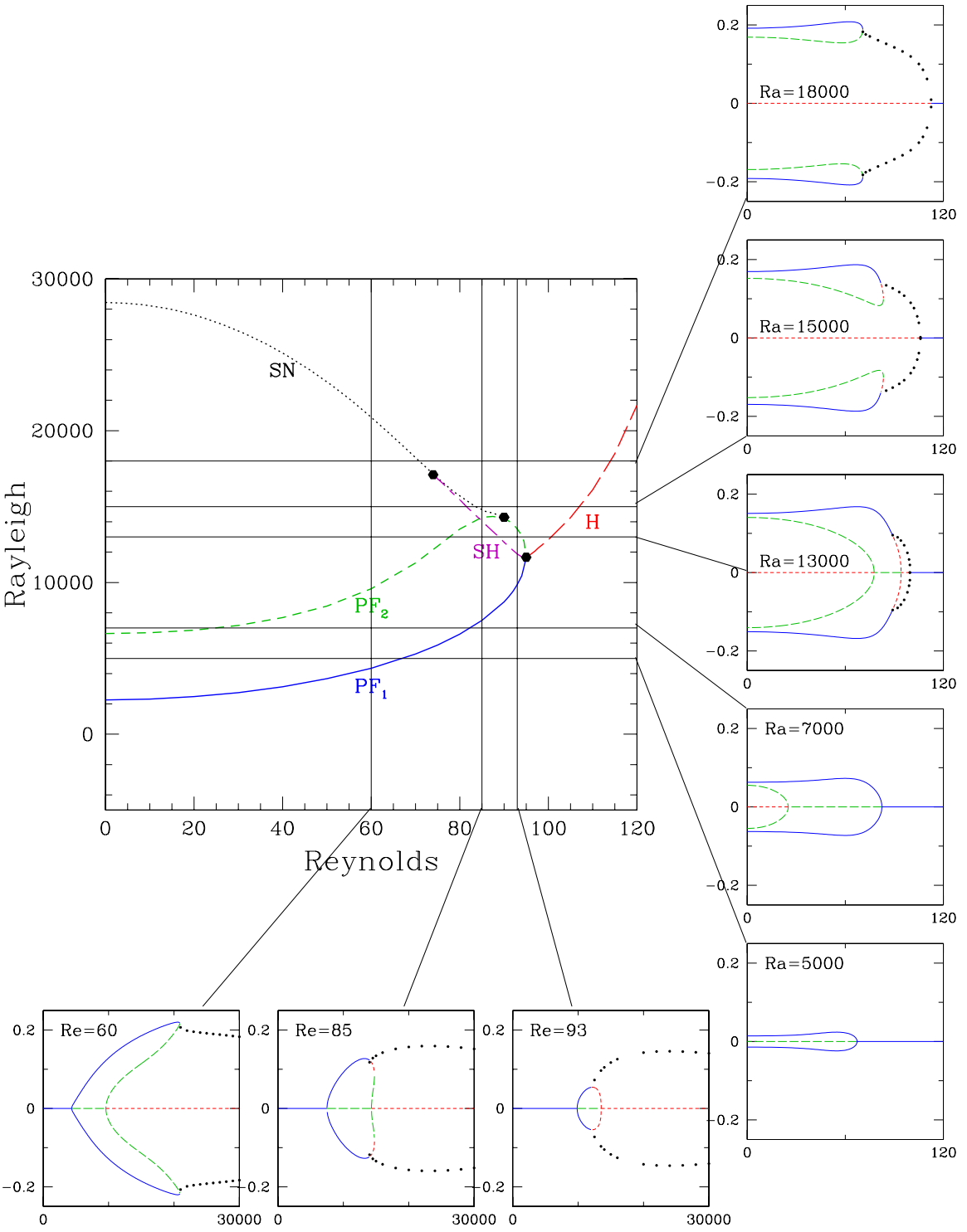

FIG. 13. (Color online) Bifurcation diagrams along lines in central (Re,Ra) diagram. $T(1/2,1/2)$ is plotted as a function of Ra for fixed Re in the diagrams along the bottom, and as a function of Re for fixed Ra in the diagrams in the column on the right. Diagrams contain steady branches with zero (blue, solid), one (green, long-dashed) and two (red, short-dashed) unstable directions. Black dots indicate limit cycles.

(viii) Ra=15 000 represents [14 300,17 100]: the two pairs of nontrivial branches are no longer connected to the trivial branch via pitchfork bifurcations, but instead arise via saddle-node bifurcations;

(ix) Ra=18 000 represents [17 100,28 445]: the secondary Hopf bifurcations have disappeared; and

(x) For Ra>28 445 (not shown), there are no nontrivial steady states, but only a limit cycle generated by the Hopf bifurcation.

(The other bifurcations depicted in the enlargement of Fig. 12, which are present for the ranges $74 \leq \mathrm{Re} \leq 95$ and $11\,750 \leq \mathrm{Ra} \leq 17\,100$, are omitted from Fig. 13 for clarity.)

Scenarios similar to those reported in this section have been computed in other hydrodynamic configurations. We review these studies and list the similarities and differences between these observations and the current results. In a cylinder with aspect ratio $\Gamma=5$, Pr=10 and thermally conducting sidewalls [7,8], steady states are produced by two pitchfork bifurcations. When Ra is increased, a SNIPER bifurcation leads to a pattern of five concentric rolls traveling radially inwards. By reducing the sidewall conductivity, other saddle-node bifurcations on the same invariant circle appeared, creating stable steady four-roll states. No Hopf bifurcations or Takens-Bogdanov points were found. Such a bifurcation may also have been responsible for long-period oscillations observed in experimental time series, but for which the flow could not be visualized [2]. A SNIPER bifurcation is also found for $\Gamma=4$, Pr=7 in a study of rotating convection [30]. When rotation is turned on, reflection symmetry (7) is broken and the pitchforks become imperfect, but the SNIPER bifurcation survives, with a limit cycle created by one saddle-node bifurcation instead of two simultaneous ones.

Siggers [9] carried out an extensive survey over $4 \leq \Gamma \leq 10$, Pr=0.1 with (less realistic but more tractable) stress-free boundary conditions. Like [34], the numerical method used an expansion in eigenfunctions of the linearized problem. In [9], 20–30 eigenfunctions were retained, a number sufficiently small to allow automatic tracking of bifurcations. A phase diagram very similar in its large-scale features to that described in this section was found: limit cycles compete with steady states that are created by two pitchfork bifurcations and destroyed by saddle-node bifurcations. However, unlike in our case, the basic state never undergoes a Hopf bifurcation like our H; the only Hopf bifurcations are those, like our SH, which create small limit cycles, like those in inset (i) of Fig. 12, sometimes called vacillation. The large limit cycle is created by neither a SNIPER nor a Hopf bifurcation, but rather by a saddle-node of periodic orbits [as in inset (j) of our Fig. 12] or by a heteroclinic bifurcation.

SNIPER bifurcations are also observed in situations with more complicated time dependence, in which the saddle-node bifurcations annihilate pairs of limit cycles to initiate flow along a torus. This is the case in a study of Rayleigh-Bénard convection with modulated rotation [31]. The basic state is a large-scale axisymmetric and reflection-symmetric time-periodic flow. As Ra or the modulation amplitude of the rotation is increased, pitchfork bifurcations produce pulsating target patterns which give way to radially traveling target patterns via a SNIPER bifurcation. Abshagen *et al.* [44,45] carried out experimental and computational studies of secondary bifurcations in Taylor-Couette flow in a small-aspect-ratio cylinder. The transitions they consider are between non-axisymmetric rotating and modulated rotating waves. However, if one of the time scales is filtered out by taking a Poincaré map and the reflection symmetry is redefined to include rotation by π around the cylinder axis, their results can be seen as entirely analogous to ours. Varying the aspect ratio and the Reynolds number, the region in which modulated rotating waves exist is bounded by curves of SNIPER and Hopf bifurcations, except over a small region in which homoclinic bifurcations and small-amplitude modulations mediate the transition.

VIII. EIGENVALUES AND EIGENVECTORS

We now focus on the behavior of the eigenvalues and eigenvectors of the basic flow as the Rayleigh and Reynolds numbers are varied. Although the linear stability analysis of a problem is usually presented before its bifurcation scenario, we will focus here on some features of the eigenvalues and eigenvectors that are independent of the bifurcation scenario.

To obtain the linear stability equations, we substitute

$$(\Psi, V_\theta, T)(r,z) + e^{\sigma t}(\psi, v_\theta, \Theta)(r,z) \tag{13}$$

into the governing Eqs. (4)–(6), where (Ψ, V_θ, T) is a steady solution of Eqs. (4)–(6), and (ψ, v_θ, Θ) is a perturbation with growth rate σ. We note that the temperature perturbation Θ is unrelated to the azimuthal angle θ while the meridional velocity perturbation is $v_r \mathbf{e}_r + v_z \mathbf{e}_z = \mathbf{e}_\theta / r \times \nabla \psi$. Retaining only the linear terms leads to

$$\sigma D^2 \psi = -(v_r \partial_- + v_z \partial_z) D^2 \Psi - (V_r \partial_- + V_z \partial_z) D^2 \psi + \left(\nabla^2 - \frac{1}{r^2}\right) D^2 \psi - \frac{\mathrm{Ra}}{\mathrm{Pr}} \partial_r \Theta + 2 \partial_z \left(\frac{V_\theta v_\theta}{r}\right), \tag{14a}$$

$$\sigma \Theta = -(v_r \partial_r + v_z \partial_z) T - (V_r \partial_r + V_z \partial_z) \Theta + \frac{1}{\mathrm{Pr}} \nabla^2 \Theta, \tag{14b}$$

$$\sigma v_\theta = -(v_r \partial_+ + v_z \partial_z) V_\theta - (V_r \partial_+ + V_z \partial_z) v_\theta + \left(\nabla^2 - \frac{1}{r^2}\right) v_\theta \tag{14c}$$

with homogeneous boundary conditions

$$\psi = \partial_z \psi = 0 \Leftrightarrow v_r = v_z = 0, \; v_\theta = 0, \; \Theta = 0 \text{ at } z = 1, \tag{15a}$$

$$\psi = \partial_z \psi = 0 \Leftrightarrow v_r = v_z = 0, \; v_\theta = 0, \; \Theta = 0 \text{ at } z = 0, \tag{15b}$$

$$\psi = \partial_r \psi = 0 \Leftrightarrow v_r = v_z = 0, \; v_\theta = 0, \; \partial_r \Theta = 0 \text{ at } r = 1, \tag{15c}$$

$$\psi = D^2 \psi = 0 \Leftrightarrow v_r = \partial_r v_z = 0, \; v_\theta = 0, \; \partial_r \Theta = 0 \text{ at } r = 0. \tag{15d}$$

The Reynolds number appears via the inhomogeneous boundary conditions on the nonlinear Eqs. (6a) and (6b), making V_θ proportional to Re. In order to make this dependence on Re explicit, we will scale V_θ (but not $V_{r,z}$ or Ψ) by Re,

$$V_\theta = \mathrm{Re} U_\theta \tag{16}$$

This scaling can be used even when Re=0 since V_θ is proportional to Re. We then rewrite Eq. (14) in a more compact matrix form as follows:

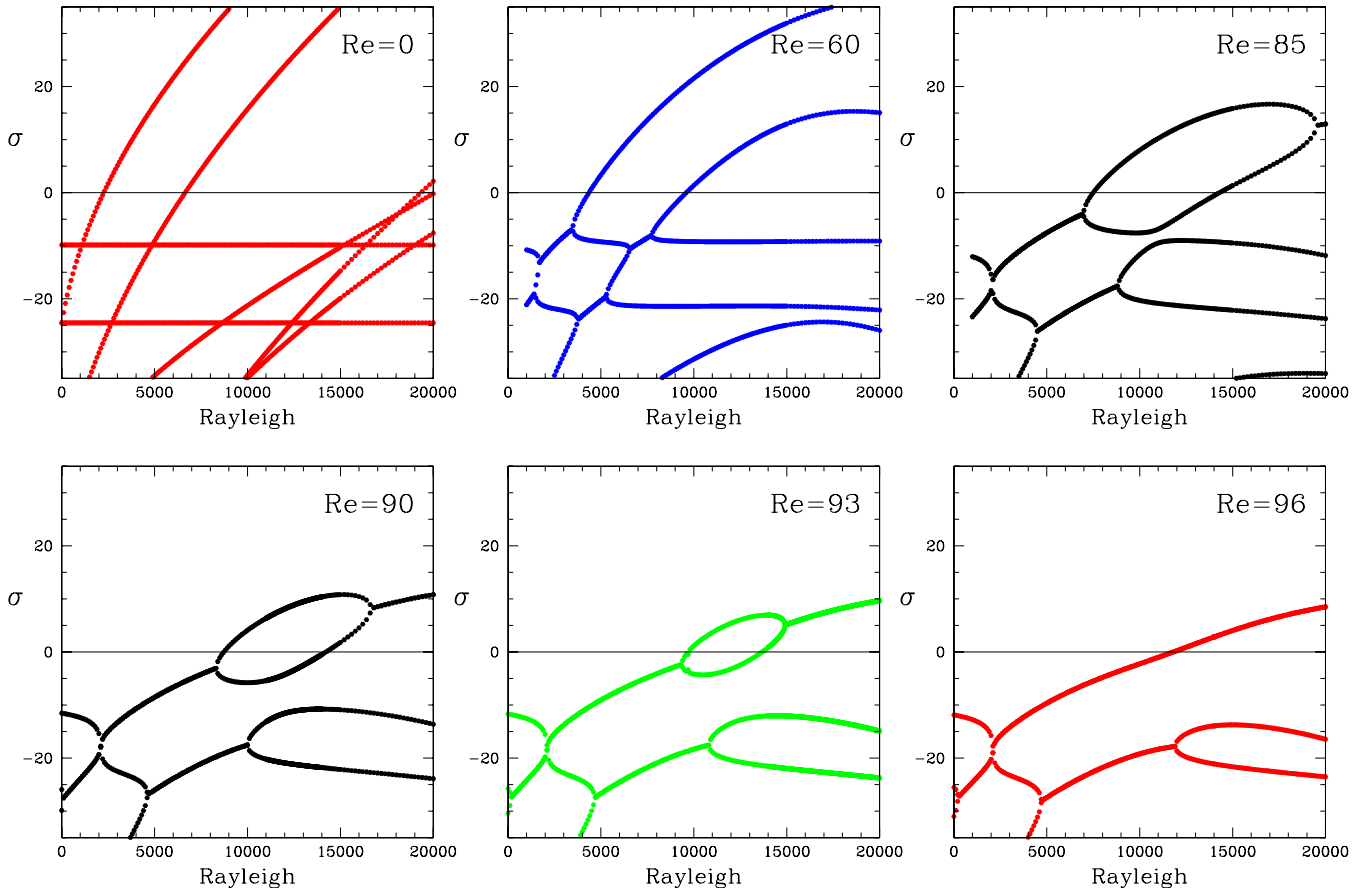

FIG. 14. (Color online) Real part σ of leading eigenvalues as a function of Ra for six values of Re. For Re=0, the eigenvalues are real and cross transversely. Zero crossings at Ra=2260 and Ra=6640 correspond to pitchfork bifurcations. Purely thermal and azimuthal eigenvalues at $\sigma=-9.87$ and $\sigma=-24.6$, respectively, are independent of Ra. When Re>0, the transverse crossings become complex-conjugate pairs, over Ra intervals which widen with increasing Re. By Re=96, the bifurcating eigenvalue is a complex-conjugate pair, leading to a Hopf bifurcation at Ra=11 856.

$$\sigma\begin{pmatrix} D^2 & 0 & 0 \\ 0 & I & 0 \\ 0 & 0 & I \end{pmatrix}\begin{pmatrix} \psi \\ \Theta \\ v_\theta \end{pmatrix} = \mathcal{L}\begin{pmatrix} \psi \\ \Theta \\ v_\theta \end{pmatrix} = \left(\begin{array}{c|cc} \mathcal{L}_{\psi\psi} & \mathcal{L}_{\psi\Theta} & \mathrm{Re}\mathcal{L}_{\psi v_\theta} \\ \hline \mathcal{L}_{\Theta\psi} & \mathcal{L}_{\Theta\Theta} & 0 \\ \mathrm{Re}\mathcal{L}_{v_\theta\psi} & 0 & \mathcal{L}_{v_\theta v_\theta} \end{array}\right)\begin{pmatrix} \psi \\ \Theta \\ v_\theta \end{pmatrix}. \tag{17}$$

The operators $\mathcal{L}_{\psi\psi},\ldots$ which comprise $\mathcal{L}$, and which depend on Re implicitly (and weakly) via the steady state, are listed below. The boxes surround terms which are nonzero when Re=0 and the steady state is the conductive solution $\mathbf{V}=0$, $T=1-z$.

$$\mathcal{L}_{\psi\psi}\psi = -\frac{1}{r}\left((\partial_z\psi)\,\partial_- - (\partial_r\psi)\,\partial_z\right) D^2\Psi - (V_r\partial_- + V_z\partial_z)\, D^2\psi + \boxed{\left(\nabla^2 - \frac{1}{r^2}\right) D^2\psi} \tag{18a}$$

$$\mathcal{L}_{\psi\Theta}\Theta = \boxed{\frac{Ra}{Pr}\partial_r\Theta} \tag{18b}$$

$$\mathcal{L}_{\psi v_\theta} v_\theta = \frac{2}{r}\partial_z(U_\theta v_\theta) \tag{18c}$$

$$\mathcal{L}_{\Theta\psi}\psi = -\frac{1}{r}(\partial_z\psi)\,\partial_r T + \boxed{\frac{1}{r}(\partial_r\psi)\,\partial_z T} \tag{18d}$$

$$\mathcal{L}_{v_\theta\psi}\psi = -\frac{1}{r}\left((\partial_z\psi)\,\partial_+ - (\partial_r\psi)\,\partial_z\right) U_\theta \tag{18e}$$

$$\mathcal{L}_{\Theta\Theta}\Theta = -(V_r\partial_r + V_z\partial_z)\,\Theta + \boxed{\frac{1}{Pr}\nabla^2\Theta} \tag{18f}$$

$$\mathcal{L}_{v_\theta v_\theta} v_\theta = -(V_r\partial_+ + V_z\partial_z)\, v_\theta + \boxed{\left(\nabla^2 - \frac{1}{r^2}\right) v_\theta} \tag{18g}$$

Figure 14 shows the real part of the leading eigenvalues (in units of the inverse viscous diffusive time) as a

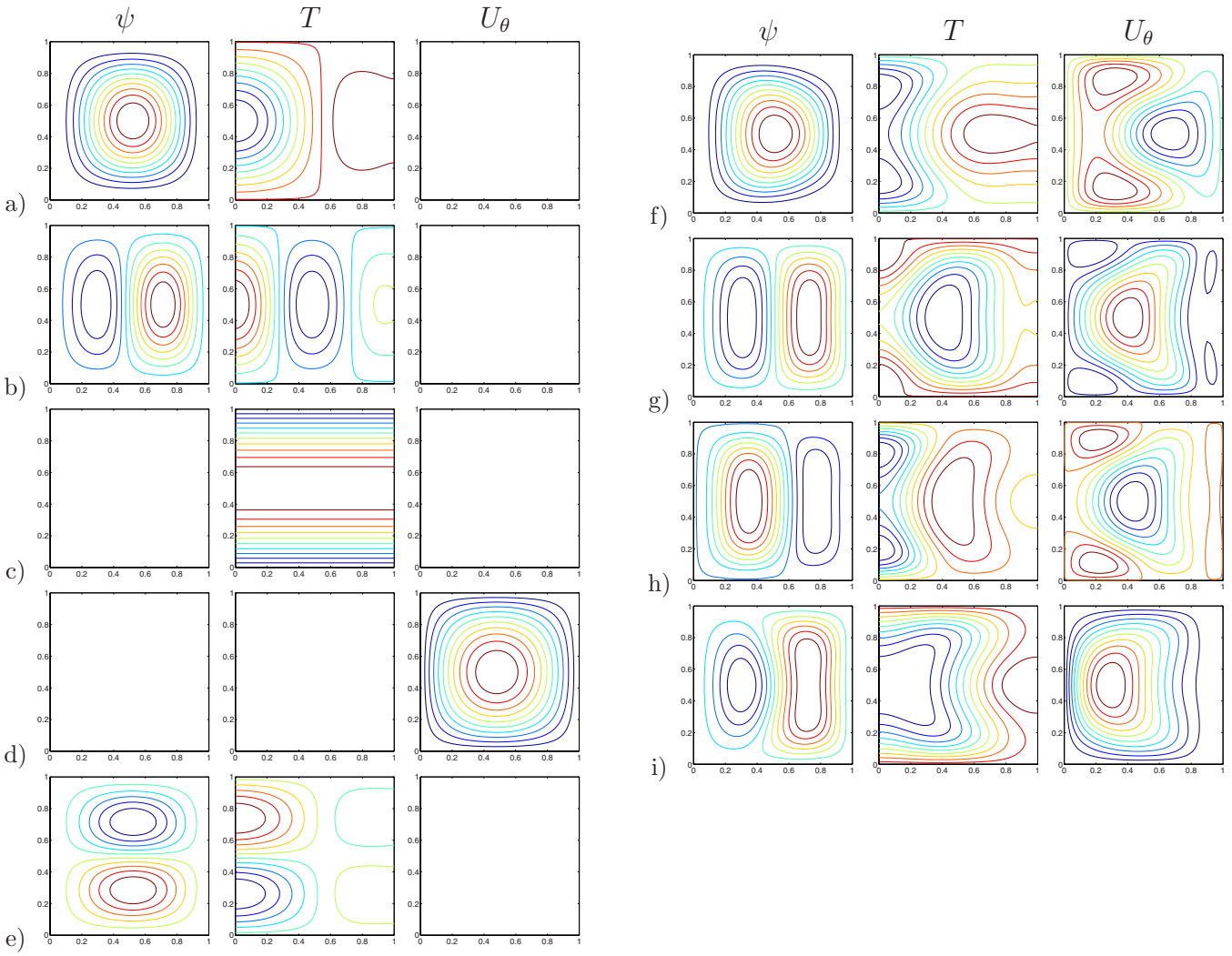

FIG. 15. (Color online) Leading eigenvectors at Ra=10 000. Left column: Re=0. (a) and (b) eigenvectors responsible for transition to convection with one and two toroidal rolls, respectively, with $\sigma=38.5$ and $\sigma=15.9$. (c) and (d) thermal and azimuthal velocity eigenvectors, respectively, with $\sigma=-9.87\approx-\pi^2$ and $\sigma=-24.6\approx-\pi^2-j_{11}^2$. (e) Eigenvector with two vertically stacked rolls, with $\sigma=-21.2$. Right column: Re=96. (f) and (g) first complex-conjugate pair, with $\sigma\pm i\omega=-2.24\pm i\,3.45$. (h) and (i) second complex-conjugate pair, with $\sigma\pm i\omega=-19.2\pm i\,4.35$.

function of Ra for several fixed values of Re, while Fig. 15 shows some of the corresponding leading eigenvectors for Re=0 and for Re=96, both for Ra=10 000. Figure 14 shows several eigenvalues which are independent of Ra when Re=0. The origin of these is well known and easily understood. For Re=0, Eqs. (17) and (18) show that the linear stability problem becomes

$$\sigma\begin{pmatrix} D^2 & 0 & 0 \\ 0 & I & 0 \\ 0 & 0 & I \end{pmatrix}\begin{pmatrix} \psi \\ \Theta \\ v_\theta \end{pmatrix} = \left(\begin{array}{c|c|c} \left(\nabla^2-\frac{1}{r^2}\right)D^2 & -\frac{\mathrm{Ra}}{\mathrm{Pr}}\partial_r & 0 \\ \hline -\frac{1}{r}\partial_r & \frac{1}{\mathrm{Pr}}\nabla^2 & 0 \\ \hline 0 & 0 & \left(\nabla^2-\frac{1}{r^2}\right) \end{array}\right)\begin{pmatrix} \psi \\ \Theta \\ v_\theta \end{pmatrix} \tag{19}$$

with the homogeneous boundary conditions [Eq. (15)]. Purely thermal eigenvectors have $\mathbf{v}=0$, leading to

$$\left.\begin{aligned} 0 &= -\frac{\mathrm{Ra}}{\mathrm{Pr}}\partial_r\Theta \\ \sigma\Theta &= \frac{1}{\mathrm{Pr}}\nabla^2\Theta \\ 0 &= \Theta|_{z=0,1} = \partial_r\Theta|_{r=0,1} \end{aligned}\right\} \Rightarrow \begin{aligned} &\Theta = \sin(k\pi z) \\ &\text{with } \sigma = -(k\pi)^2 . \end{aligned} \tag{20}$$

The first of these thermal eigenvalues is seen in Fig. 14 (Re=0) as the horizontal line very close to its analytic value of $-\pi^2=-9.8696$. The corresponding thermal eigenvector is shown in Fig. 15(c). Another set of solutions contains only azimuthal velocity: with $\Theta=\psi=0$ and v_θ a solution to

$$\left.\begin{aligned} \sigma v_\theta &= \left(\nabla^2 - \frac{1}{r^2}\right)v_\theta \\ 0 &= v_\theta|_{z=0,1} = v_\theta|_{r=0,1} \end{aligned}\right\} \Rightarrow \begin{aligned} &v_\theta = \sin(k\pi z)J_1(rj_{1n}) \\ &\text{with } \sigma = -((k\pi)^2 + j_{1n}^2) \end{aligned} \tag{21}$$

where J_1 is the first Bessel function and $j_{1n}=3.8317, 7.0156, \ldots$ is one of the zeros of J_1. The first of these azimuthal velocity eigenvalues is the horizontal line seen in Fig. 14 (Re=0), again very close to its analytically computed value of $-(\pi^2+3.8317^2)=-24.551$. The corresponding azimuthal velocity eigenvector is shown in Fig. 15(d).

The other eigenvalues shown in Fig. 14 (Re=0) increase with Ra. The zero crossings of the two largest eigenvalues are associated with the pitchfork bifurcations discussed extensively in the previous section; these take place at Ra =2260 and Ra=6640. Their associated eigenvectors are shown in Figs. 15(a) and 15(b), for Ra=10 000, where their eigenvalues are 38.5 and 15.9, and they are seen to contain one and two concentric radial rolls, respectively. The leading eigenvectors for higher Re are similar. The convective states in Figs. 5 and 6 do not resemble Fig. 15(a), even though they result from a pitchfork bifurcation involving this eigenvector. This is because the nonlinear steady states in Figs. 5 and 6 are a superposition of these eigenvectors and the basic flows shown in Figs. 3 and 4. The eigenvector in Fig. 15(e), with two vertically stacked rolls, is associated with eigenvalue σ =−21.2, between that of the thermal and azimuthal eigenvalues at Re=10 000.

An overall feature of the eigenvalues for Re=0 that can be seen in Fig. 14 is that they are all real and cross transversely. Indeed, it is well known that for Rayleigh-Bénard convection (i.e., Re=0), all of the eigenvalues are real. When Re>0, the eigenvalue crossings which occur for Re=0 become complex-conjugate pairs. (Because the real parts of the eigenvalues are shown in Fig. 14, complex-conjugate pairs appear as a fusion of two eigenvalue curves.) As Re increases, the Ra intervals over which the eigenvalues are complex widen. By Re=96, the real eigenvalues responsible for the pitchfork bifurcations have merged into a complex-conjugate pair whose real part crosses zero at Ra=11 856 at the Hopf bifurcation point. At Re=95 (not shown), the fusion of two real eigenvalues into a complex-conjugate pair and the zero crossing occur simultaneously at Ra=11 750: this is the Takens-Bogdanov codimension-two point.

Figures 15(f) and 15(g) shows the real and imaginary part of the complex-conjugate pair which is the leading eigenvector for Re=96. The fact that this complex pair at Re=96 originates in the fusion of the leading real eigenvectors at lower Re is made strikingly clear when the streamfunctions ψ in Figs. 15(f) and 15(g) are compared with those of Figs. 15(a) and 15(b). Note that the choice of the real and imaginary parts of an eigenvector is arbitrary, since an eigenvector can be multiplied by any complex number. The particular choice here is imposed by the normalization $\mathcal{I}m[\psi(r=1/2,\ z=1/2)]=0$. The decomposition of the complex eigenvector ψ into two vectors containing one and two concentric radial rolls shows that the limit cycle will involve competing radial structures. As with the steady states, the lack of resemblance between Figs. 15(f) and 15(g) and the limit cycle in Fig. 7 is due to the fact that these are superpositions of the basic state and the eigenvectors.

We investigate the progression of the eigenvalues from real to complex as Re increases by examining the matrix in Eq. (17), which is block diagonal for Re=0, as shown in Eq. (19). Its eigenvalues and eigenvectors thus consist of two sets: those of the thermal convection problem (upper left submatrix) and those of the azimuthal problem (lower right submatrix). The convective, thermal and azimuthal eigenvalues cross transversely because Eq. (19) has no off-diagonal terms and because the eigenvalues within each of these subproblems, each associated with a different spatial structure, do not cross one another.

This behavior resembles that seen near the Takens-Bogdanov point which occurs in binary fluid or thermosolutal convection. In the binary/thermosolutal case, the pair of eigenvectors which interact have different origins: one can be viewed as arising primarily from thermal convection and the other from solutal convection [46]. In the Rayleigh-Bénard/von Kármán case studied here, the eigenvectors which become complex both arise from thermal convection; the difference between them is their spatial structure, shown in Figs. 15(a) and 15(b).

In the binary/thermosolutal case, the transverse crossings undergo two different fates, depending on the sign of the separation parameter S, which describes whether the thermal and solutal convection act in concert or in opposition. For positive S, the eigenvalue curves separate into two hyperbolas, in what is called avoided crossings, and remain real. For negative S, the eigenvalues join in complex-conjugate pairs, as in Fig. 14. These two cases can be understood in terms of a 2×2 matrix, whose off-diagonal terms are of the same sign if S is positive and of opposite signs if S is negative. Here, we have not attempted such an analysis, but we can conclude that the off-diagonal matrices

$$\begin{pmatrix} \mathrm{Re}\mathcal{L}_{\psi v_\theta} \\ 0 \end{pmatrix} \quad \text{and} \quad \begin{pmatrix} \mathrm{Re}\mathcal{L}_{v_\theta\psi} & 0 \end{pmatrix} \tag{22}$$

are in some sense of opposite signs, since the coupling they cause between the convective and azimuthal velocity eigenvectors leads to complex eigenvalues. The coupling between the convective and the purely thermal eigenvectors must also be of this type. In [46], a calculation of the sign of the coupling terms is presented for the binary/thermosolutal case, involving projecting onto the eigenvectors of the diagonal submatrices.

IX. DISCUSSION

We have shown that a transition analogous to the onset of convection occurs in an axisymmetric cylindrical container subjected to vertical gradients in temperature and azimuthal velocity, i.e., in Rayleigh-Bénard/von Kármán flow. Differential rotation, which causes mixing via Ekman pumping, delays the onset of convection. The transition is a pitchfork bifurcation, leading to steady convection, for $\mathrm{Re} < 95$ and a Hopf bifurcation, leading to oscillatory convection, for $\mathrm{Re} > 95$. Between these two types of convection, over most of the $(0 \leq \mathrm{Re} \leq 120, 0 \leq \mathrm{Ra} \leq 30\,000)$ parameter space, the transition occurs via a SNIPER bifurcation, in which the stable steady states meet a pair of unstable steady states and mutually annihilate, leaving a limit cycle in their wake. Over a small portion of the parameter space, the scenario is more complicated and involves several global bifurcations. (Section IV mentions some consequences of relaxing the imposition of axisymmetry.)

The linear stability analysis of the axisymmetric Rayleigh-Bénard/von Kármán problem also shows interesting features. We have traced the way in which differential rotation couples the eigenvalue branches, which are real for Rayleigh-Bénard convection, in such a way that they become complex. The close resemblance between the leading real pair of eigenmodes for $\mathrm{Re} < 95$ and the leading complex pair for $\mathrm{Re} > 95$ supports the idea that a common basis of eigenvectors could be used to make the reduced model studied in the companion paper [34] more economical.

Since its discovery by Andronov and Leontovich [41], the SNIPER bifurcation has appeared in a number of ODE systems used to model chemical reactions, notably in excitable media and the Belousov-Zhabotinsky reaction [47], and population biology, for example predator-prey systems. In the hydrodynamic and PDE context, the SNIPER bifurcation was observed in simulations of axisymmetric Rayleigh-Bénard convection [7,8,30,31]. Convective states with different radial wavelengths compete, much as occurs in the present Rayleigh-Bénard/von Kármán configuration. The closest analogy with the bifurcation scenario we observe is found in the small-aspect-ratio study of Taylor-Couette flow by [44,45], in which rotating and modulated rotating waves play the role of our steady states and limit cycles, respectively.

Recently, the SNIPER bifurcation has been the subject of renewed attention as a possible explanation for the reversals of the earth's magnetic field. A dynamo engendered by bulk fluid motion was first produced in a laboratory experiment of the von Kármán flow in sodium (VKS), an electrically conducting fluid [19]. This VKS experiment shows reversals of the polarity of the magnetic field which bear some similarity to that of the terrestial field. An explanation involving a SNIPER bifurcation in a low-dimensional dynamical system with noise has been put forward to explain these reversals [20,21]. This manifestation of the SNIPER bifurcation also provides some possible justifications for studying the axisymmetric flow. In the VKS experiment, the mean of the highly turbulent flow is axisymmetric, even though the instantaneous flow is not. A different mechanism for magnetic field reversals has been proposed [48], in which noise is added to a low-dimensional dynamical system displaying a Takens-Bogdanov point. The Takens-Bogdanov point, separating a steady from a Hopf bifurcation point, also plays an essential role in our system, as it does in the investigations of axisymmetric Rayleigh-Bénard convection by [9] and of Taylor-Couette flow by [44,45]. It seems plausible that the TB point and the hysteresis point terminating the SNIPER bifurcation curve form part of the unfolding of a codimension-three point.

Our study was first intended to determine the effect of the von Kármán flow on the onset of Rayleigh-Bénard convection. Over the course of the investigation, we encountered a bifurcation scenario leading to oscillations, which should and does occur quite generally, whenever consecutive pitchfork bifurcations take place. It should therefore be of interest to the dynamical-systems community as well as to fluid dynamicists.

[1] G. Charlson and R. Sani, Int. J. Heat Mass Transfer **14**, 2157 (1971).

[2] R. P. Behringer, H. Gao, and J. N. Shaumeyer, Phys. Rev. Lett. **50**, 1199 (1983).

[3] J. Buell and I. Catton, ASME J. Heat Transfer **105**, 255 (1983).

[4] M. Wanschura, H. C. Kuhlmann, and H. J. Rath, J. Fluid Mech. **326**, 399 (1996).

[5] R. Touihri, H. Ben Hadid, and D. Henry, Phys. Fluids **11**, 2078 (1999).

[6] K. Borońska and L. S. Tuckerman, J. Fluid Mech. **559**, 279 (2006).

[7] L. S. Tuckerman and D. Barkley, Phys. Rev. Lett. **61**, 408 (1988).

[8] D. Barkley and L. S. Tuckerman, Physica D **37**, 288 (1989).

[9] J. H. Siggers, J. Fluid Mech. **475**, 357 (2003).

[10] Y. A. Gelfgat, P. Z. Bar-Yoseph, and A. Solan, Phys. Fluids **8**, 2614 (1996).

[11] J. M. Lopez, J. Fluid Mech. **359**, 49 (1998).

[12] J. M. Lopez, J. E. Hart, F. Marques, S. Kittelman, and J. Shen, J. Fluid Mech. **462**, 383 (2002).

[13] F. Marques, A. Y. Gelfgat, and J. M. Lopez, Phys. Rev. E **68**, 016310 (2003).

[14] C. Nore, L. S. Tuckerman, O. Daube, and S. Xin, J. Fluid Mech. **477**, 51 (2003).

[15] C. Nore, M. Tartar, O. Daube, and L. S. Tuckerman, J. Fluid Mech. **511**, 45 (2004).

[16] C. Nore, L. Martin Witkowski, E. Foucault, J. Pécheux, O. Daube, and P. Le Quéré, Phys. Fluids **18**, 054102 (2006).

[17] S. Douady, Y. Couder, and M. E. Brachet, Phys. Rev. Lett. **67**, 983 (1991).

[18] F. Ravelet, L. Marié, A. Chiffaudel, and F. Daviaud, Phys. Rev.

Lett. **93**, 164501 (2004).
[19] M. Berhanu, R. Monchaux, S. Fauve, N. Mordant, F. Pétrélis, A. Chiffaudel, F. Daviaud, B. Dubrulle, C. Gasquet, L. Marié, F. Ravelet, M. Bourgoin, Ph. Odier, M. Moulin, J.-F. Pinton, and R. Volk, EPL **77**, 59001 (2007).
[20] F. Ravelet, M. Berhanu, R. Monchaux, S. Aumaitre, A. Chiffaudel, F. Daviaud, B. Dubrulle, M. Bourgoin, P. Odier, N. Plihon, J. F. Pinton, R. Volk, S. Fauve, N. Mordant, and F. Petrelis, Phys. Rev. Lett. **101**, 074502 (2008).
[21] F. Pétrélis, S. Fauve, E. Dormy, and J.-P. Valet, Phys. Rev. Lett. **102**, 144503 (2009).
[22] X. Nicolas, Int. J. Therm. Sci. **41**, 961 (2002).
[23] R. M. Clever and F. H. Busse, J. Fluid Mech. **229**, 517 (1991).
[24] R. M. Clever and F. H. Busse, J. Fluid Mech. **234**, 511 (1992).
[25] H. W. Müller, M. Lücke, and M. Kamps, Phys. Rev. A **45**, 3714 (1992).
[26] V. Lepiller, A. Goharzadeh, A. Prigent, and I. Mutabazi, Eur. Phys. J. B **61**, 445 (2008).
[27] R. Tagg and P. D. Weidman, Z. Angew. Math. Phys. **58**, 431 (2007).
[28] J. M. Owen and R. H. Rogers, *Flow and Heat Transfer in Rotating-Disk Systems, Rotor-Stator Systems* (Wiley, New York, 1989), Vol. 1.
[29] E. Knobloch, Int. J. Eng. Sci. **36**, 1421 (1998).
[30] J. M. Lopez, A. Rubio, and F. Marques, J. Fluid Mech. **569**, 331 (2006).
[31] A. Rubio, J. M. Lopez, and F. Marques, J. Fluid Mech. **608**, 357 (2008).
[32] C. Y. Soong, Int. J. Heat Mass Transfer **39**, 1569 (1996).
[33] R. W. Hill and K. S. Ball, Int. J. Heat Fluid Flow **20**, 208 (1999).
[34] M. C. Navarro, L. Martin Witkowski, L. S. Tuckerman, and P. Le Quéré, Phys. Rev. E **81**, 036323 (2010).
[35] S. V. Patankar, *Numerical Heat Transfer and Fluid Flow* (Hemisphere Publishing, Newport, Australia, 1980).
[36] L. M. Witkowski, P. Marty, and J. S. Walker, J. Fluid Mech. **436**, 131 (2001).
[37] E. J. Doedel, *Survey Lectures on "Nonlinear Systems of Equations,"* Lecture Notes on "Numerical Analysis of Bifurcation Problems" (Spring School on Numerical Software, Hamburg, Germany, 1997).
[38] W. J. F. Govaerts, *Numerical Methods for Bifurcations of Dynamical Equilibria* (SIAM, Philadelphia, 2000).
[39] M. C. Navarro, A. M. Mancho, and H. Herrero, Chaos **17**, 023105 (2007).
[40] B. C. Houchens, L. Martin Witkowski, and J. S. Walker, J. Fluid Mech. **469**, 189 (2002).
[41] A. Andronov and E. Leontovich, Uchen. Zap. Gork. Univ. **6**, 3 (1939).
[42] Y. Kuznetsov, *Elements of Applied Bifurcation Theory* (Springer, New York, 1998).
[43] V. Arnold, *Geometrical Methods in the Theory of Ordinary Differential Equations* (Springer, New York, 1982).
[44] J. Abshagen, J. M. Lopez, F. Marques, and G. Pfister, Phys. Rev. Lett. **94**, 074501 (2005).
[45] J. Abshagen, J. M. Lopez, F. Marques, and G. Pfister, J. Fluid Mech. **540**, 269 (2005).
[46] L. S. Tuckerman, Physica D **156**, 325 (2001).
[47] J. Guckenheimer, Physica D **20**, 1 (1986).
[48] F. Stefani and G. Gerbeth, Phys. Rev. Lett. **94**, 184506 (2005).